Soft Matter

Soft, Flexible Pressure Sensors for Pressure Monitoring Under Large Hydrostatic Pressure and Harsh Ocean Environments

Journal:	*Soft Matter*
Manuscript ID	SM-ART-04-2023-000563.R1
Article Type:	Paper
Date Submitted by the Author:	21-Jun-2023
Complete List of Authors:	Li, Yi; University of Connecticut, Materials Science and Engineering Villada, Andres; University of Colorado Boulder Lu, Shao-Hao; University of Connecticut, Department of Materials Science and Engineering Sun, He; University of Connecticut Xiao, Jianliang; University of Colorado, Department of Mechanical Engineering Wang, Xueju; University of Connecticut, Materials Science and Engineering

Title: Soft, Flexible Pressure Sensors for Pressure Monitoring Under Large Hydrostatic Pressure and Harsh Ocean Environments

Yi Li[a#], Andres Villada[b#], Shao-Hao Lu[a], He Sun[c], Jianliang Xiao[b], Xueju Wang[a,d]**

[a] Department of Materials Science and Engineering, University of Connecticut, Storrs, CT 06269, USA

[b] Department of Mechanical engineering, University of Colorado, Boulder, CO 80309, USA

[c] Department of Biomedical Engineering, University of Connecticut, Storrs, CT 06269, USA

[d] Institute of Materials Science, University of Connecticut, Storrs, CT 06269, USA

*Corresponding author. Email: xueju.wang@uconn.edu; jianliang.xiao@colorado.edu

# Yi Li and Andres Villada contributed equally to this paper.

Abstract

Traditional rigid ocean pressure sensors typically require protection from bulky pressure chambers and complex seals to survive the large hydrostatic pressure and harsh ocean environment. Here we introduce soft, flexible pressure sensors that can eliminate such need and measure a wide range of hydrostatic pressure (0.1 MPa to 15 MPa) in environments that mimic the ocean, achieving small size, high flexibility, and potentially low power consumption. The sensors are fabricated from lithographically patterned gold thin films (100 nm thick) encapsulated with a soft Parylene C film and tested in a customized pressure vessel with well-controlled pressure and temperature conditions. Using a rectangular pressure sensor as an example, the resistance of the sensor is found to decrease linearly with the increase of the hydrostatic pressure from 0.1 MPa to 15 MPa. Finite element analysis (FEA) reveals the strain distribution in the pressure sensor under hydrostatic pressure of up to 15 MPa. The effect of geometry on sensor performance is also studied, and symmetric pressure sensors (like circular and spike-shaped) are shown to have more uniform strain distributions under large hydrostatic pressure and, therefore, a potentially enhanced pressure measurement range. Pressure sensors of all geometries show high consistency and negligible hysteresis over 15 cyclic tests. In addition, the sensors exhibit excellent flexibility and operate reliably under a hydrostatic pressure of 10 MPa for up to 70 days. The developed soft pressure sensors are promising for integration with many platforms including animal tags, diver equipment, and soft underwater robotics.

1. Introduction

With the rapid development of sensing technology, pressure sensors have been used in many fields including health monitoring[1-3], ocean exploring robots[4-6] and ocean animal tags[7-9]. For example, pressure sensors in conductivity-temperature-depth (CTD) sensor systems are used to monitor parameters like ocean depth and water velocity[10-14] in the ocean, which usually requires that the sensor withstands large hydrostatic pressure. Traditional ocean pressure sensors such as those in cable-controlled underwater vehicles[15, 16] and rigid underwater robots[6, 17, 18] are made of rigid metals (e.g., high-strength stainless steel), which often need the protection of a pressure chamber to survive the large hydrostatic pressure in the ocean, limiting the flexibility of the sensing systems for integration with many platforms and increasing the size and energy consumption of the sensor system[19, 20].

In the past decade, many flexible pressure sensors have been developed based on soft materials including polydimethylsiloxane (PDMS)[21, 22], hydrogels[23-25], liquid crystal polymers (LCPs)[26, 27], and dielectric elastomers[28, 29]. The flexible pressure sensors based on soft materials are promising for deep ocean sensing because of their incompressibility under large hydrostatic pressure and, therefore, the elimination of pressure chambers. However, the study on the measurement range of these flexible pressure sensors so far is mostly limited to the order of a few kPa, rarely reaching the range of MPa[30, 31]. For example, a pressure sensor with microstructured rubber dielectric layers for electronic skin has a pressure measuring range under 100 kPa[28]. More recently, a porous PDMS-based flexible pressure sensor for autonomous underwater vehicles is reported with the pressure measurement range of 0-230 kPa[32]. To further

expand the potential applications of flexible electronics to a deep ocean environment, desired sensors are expected to have robust performance including high sensitivity and high stability over a wide range of hydrostatic pressure (e.g., on the order of a few or tens of MPa)[7-9, 33]. For example, in our previous studies[33, 34], we introduced soft, pressure-tolerant temperature and salinity sensors with high flexibility for operating in large hydrostatic pressure (0.1-15 MPa) and high salinity (30-40 Practical Salinity Unit (PSU)) environments, thus eliminating the need for the protection from pressure chambers and potentially achieving low power consumption.

Here we develop soft, flexible pressure sensors that can measure large hydrostatic pressures of up to 15 MPa via an integrated experimental and computational approach. The pressure sensor consists of ultra-thin gold (Au) films encapsulated with soft Parylene C films for depth measurements in marine environments. Pressure sensors with three types of geometries (rectangular, circular, and spike) are designed and tested in a custom-built pressure vessel to mimic the ocean environment. The resistance values of the pressure sensors are linearly proportional to the change of hydrostatic pressure (0.1-15 MPa), which shows excellent consistency with simulation results via finite element analysis (FEA). In addition, the symmetric geometry (circular- and spike-shaped pressure sensors) can alleviate stress concentrations under large hydrostatic pressure, thereby improving the sensitivity and measurement range of the sensor. These pressure sensors exhibit excellent cyclic loading behavior under varying hydrostatic pressure of 0.1-15 MPa and negligible hysteresis. In addition, they show insensitivity to bending curvatures of 0-6.18 m^{-1}, and present high stability during cyclic bending tests (10,000 cycles), demonstrating high flexibility. Encapsulated

sensors with transparent Parylene C [35-37] films are shown to survive the 10 MPa pressure environment for more than 70 days, demonstrating excellent encapsulation capability under large hydrostatic pressure and harsh environment.

2. Results and Discussion

2.1 Design and fabrication of soft pressure sensors for ocean sensing

The schematic illustration in **Figure 1A** presents the basic idea of the developed soft pressure sensors that can be conformally integrated with various platforms at different depths of the ocean, such as divers for health monitoring (0-50 m), soft marine robots exploring the ocean (0-500 m), and marine animals to track their behaviors (0-1 km). The pressure sensor consists of a thin gold layer (Au, 100 nm thick)[38] prepared via magnetron sputtering (AJA Orion-8 Magnetron Sputtering System, AJA International Inc.) of Au onto a polyimide (PI, 7.6 μm) substrate, with a thin adhesion layer of chromium (Cr, 10 nm) between Au and PI (**Figure 1B**). The Au/Cr thin film is subsequently patterned into narrow traces (42 μm wide) in serpentine geometry via photolithography to enhance its stretchability. To encapsulate the Au conductive traces, another PI layer (7.6 μm) is deposited on top of Au, followed by the encapsulation with a Parylene C layer (6 μm thick, Specialty Coating System, Inc.). The thin Parylene C coating (see details in the Experimental Section) provides a number of useful properties including excellent water and ion barrier properties, chemical and dielectric barrier properties, and, therefore, serves as an enhanced encapsulation layer for pressure sensors to operate in the harsh ocean environment [39-41]. The effective modulus of this multi-layer sensor is evaluated to be 3.66 GPa (**Table S1** and **Supplementary Note 1**), which is comparable to that of typical polymers

like polyimide[42-44] and SU-8[45-47].

2.2 Characterization and testing of the soft pressure sensor

Figure 2A shows that the pressure sensor integrated onto a PDMS substrate is bent by two hands, exhibiting great flexibility. The zoom-in optical microscope image demonstrates the high transparency of the Parylene C encapsulation layer, which allows monitoring the morphology of the sensor during operation as well as before and after testing. To evaluate the performance of the sensor under large hydrostatic pressure, we test the sensor in a customized pressure vessel (maximum pressure: 3000 psi; Pharr Instrument Company, Moline, IL) under a hydrostatic pressure range of 0.1-15 MPa, corresponding to an ocean depth of 0-1.5 km. Meanwhile, a three-dimensional (3D) finite element model of the pressure sensor is created using Abaqus software (Dassault Systèmes) (see details in the Experimental Section) to predict the strain distribution within the sensor. The model uses compressive stress/strain data input to capture the elastic response of Parylene C to large compressive forces. The encapsulation layer, Parylene C, is modeled as 3D, hybrid, reduced integration elements while the other layers that comprise the sensor are modeled as shells to simplify the contact between interfaces at small strains, with the various sensor layers assigned their respective material properties and thicknesses (see **Table S1**). The properties of the Au layer are assumed to be those of a thin film nanocrystalline Au film with a grain size of 40 nm[48, 49]. The bottom of the device is prevented from being displaced by an encastre boundary condition to model the sensor being adhered with no slipping on a rigid surface, and hydrostatic pressure of up to 15 MPa is applied on the remaining surfaces of the device.

Figure 2B shows that the fractional resistance change of the pressure sensor decreases linearly from 0% to -0.568% as the hydrostatic pressure increases from 0.1 MPa to 15 MPa. Please note that R_0 is the resistance of the pressure sensor at 0.1 MPa, and $\triangle R$ represents the difference between the resistance value (R) of the sensor and R_0. The modeling (blue dots) and experimental (black dots) results agree well. **Figure 2C** and **Figure S1** show the predicted strain distribution within the sensor under hydrostatic pressure of 1-15 MPa via FEA simulations. We can see that the strain distribution is relatively uniform under low hydrostatic pressures (1-3 MPa), but the strain distribution under high pressure levels shows that strain starts to concentrate on certain Au traces as the pressure increases due to out-of-plane deformation of the sensor under hydrostatic compression.

We further test the cyclic loading behavior of the sensor under hydrostatic pressure levels of 0.1 MPa-15 MPa. It can be seen that the sensor exhibits negligible hysteresis during loading and unloading, with no visible changes in the morphology of the sensor as shown in the inserts of **Figure 2D**. The reliability and repeatability of the sensor are further demonstrated in additional cyclic loading/unloading tests (15 cycles) (Figure 2E and Figure S2), where the sensor functions well with no visible morphology changes after the cyclic testing. In addition, to quantitatively evaluate the flexibility of the pressure sensor, we conformally laminate the sensor onto 3D printed arched molds made of digital ABS (Form 3+ SLA 3D printer; angles: 0^o-50^o) and record the resistance change of the sensor under various bending curvatures of 0-6.18 m^{-1}. **Figure 2F** demonstrates that the resistance of the pressure sensor is insensitive to the curvature change, with high repeatability (standard deviation s= 0.038%; n=3). Here R_0 is the resistance of the pressure sensor in the flat state (zero curvature), and $\triangle R$ represents the

difference between the resistance value (R) of the sensor and R_0. Furthermore, we perform cyclic bending test (CellScale, Univert, at a loading rate of 0.5 mm/s at room temperature) of the sensor. As shown in Figure 2G, the sensor shows high reliability with negligible hysteresis resistance changes of up to 0.0371% over 1000 cycles of bending tests. Here, similarly, R_0 is the resistance of the pressure sensor before the cyclic bending test (under zero loading).

2.3 Effect of geometry on the performance of pressure sensors

The nonuniform strain distribution in the rectangular pressure sensor under large hydrostatic pressure discussed above may lead to plastic deformation in the strain-concentrated region and, therefore, limit the pressure measurement range of the sensor. To explore the effect of geometry designs on the performance of pressure sensors, we further fabricate pressure sensors of two additional symmetric geometries: circular and spike shapes. Firstly, we design a circular pressure sensor that consists of narrow Au traces (same width as that of rectangular pattern) following the experimental procedure described in section 2.1 to reduce sharp corners and avoid stress concentrations. **Figure 3A** shows that the fractional resistance change of the circular pressure sensor varies linearly to a value of -0.496% as hydrostatic pressure increases from 0.1 MPa to 15 MPa, with excellent consistence between modeling (the blue plots) and experimental (the red plots) results. In addition, the FEA-predicted strain distributions of the circular pressure sensor under hydrostatic pressure of 1-15 MPa, as shown in **Figure 3B**, and **Figures S3** and **S7**, are relatively uniform compared with that of the rectangular pressure sensor due to the radially symmetric deformation in the sensor material caused by the hydrostatic pressure. **Figure 3C** shows the fractional resistance change of the circular pressure sensor under the loading/unloading cyclic test (15 cycles, pressure range: 0.1 MPa-15 MPa), which indicates

that the performance of this circular pressure sensor is highly repeatable and reliable. The comparison between optical microscope images before and after testing in **Figure S4** also demonstrates that there is no significant change in the morphology of the sensor after testing. In addition, the cyclic bending test results of the circular pressure sensor in Figure 3D show the high stability of the sensor performance with negligible hysteresis resistance change (0.0459%) during cyclic bending tests (1000 cycles). Here R_0 is the resistance of the pressure sensor before the cyclic bending test (under zero loading). We further design a pressure sensor with spike patterns of narrower Au traces (width: 34 μm), which has shown a resistance change of 0.439% over a pressure increase of 0.1 MPa-15 MPa (**Figure 3E**). The experimental plot also shows excellent consistency with simulation results, where strain distributions of the radially symmetric spike-shape pressure sensor (**Figure 3F**, **Figure S6** and **Figure S7**) keep relatively uniform as the pressure increases from 0.1 MPa to 15 MPa. In addition, the spike-shaped pressure sensor also exhibits high reliability and repeatability under cyclic loading (**Figure 3G** and **Figure S8)** and bending tests (**Figure 3H**), with no visible morphological changes after the cyclic and bending tests. In particular, **Figure 3H** shows negligible hysteresis resistance change of 0.0263%, where R_0 is the resistance of the pressure sensor before the cyclic bending. These results demonstrate that the two types of pressure sensors in symmetric geometry provide more uniform strain distributions under large hydrostatic pressure and, therefore, are potentially more mechanical robust for measuring a wide range of hydrostatic pressure in the ocean environment.

2.4 Encapsulation of pressure sensors for ocean sensing

As mentioned earlier, a Parylene C layer is applied on the fabricated resistive pressure sensor to improve the encapsulation capability especially under harsh ocean environments. **Figure 4A**

presents the fractional resistance change of a rectangular pressure sensor that is encapsulated with Parylene C (6 μm) and monitored in the pressure vessel filled with deionized (DI) water under a hydrostatic pressure of 10 MPa. The sensor has negligible resistance changes over 72 days, which shows the excellent encapsulation capability of the Parylene C layer for operation in large hydrostatic pressure. The optical microscope image of the sensor after testing in **Figure 4B** shows that the damage of the sensor beyond 72 days is probably caused by cracking in Au traces. To further evaluate the encapsulation capability of the Parylene C layer in the salinity environment, we test pressure sensors encapsulated with Parylene C and PDMS (for control study), respectively, in 35 PSU NaCl solution in the pressure vessel (10 MPa) to monitor their performance. PDMS-encapsulated sensors are used for control studies here because PDMS has been widely used in the encapsulation of flexible electronics as wearable or implantable devices, due to its thermal and electrical insulation capability and biocompatibility[50-52]. Figure 4C shows that the resistance of the two PDMS-encapsulated pressure sensors starts to increase abruptly on day 9 and day 14, respectively, while the Parylene C-encapsulated pressure sensor can maintain stable performance for up to 21 days (see Figure 4D). The results demonstrate the Parylene C-coated pressure sensor has a significantly improved encapsulation capability.

3. Conclusion

To sum up, the integrated experimental and simulation study of the developed soft, flexible pressure sensors reveals reliable sensor performance for sensing under large hydrostatic pressure and harsh ocean environments. Fabricated from ultra-thin gold films, the pressure sensors exhibit high linearity in resistance changes under the pressure increase from 0.1 MPa

to 15 MPa. In addition, there is negligible hysteresis during the cyclic loading/unloading test of the sensor, and high flexibility is demonstrated during the cyclic bending test of up to 10000 cycles of the sensor. Pressure sensors of symmetric geometries enable more uniform strain distributions under large hydrostatic pressure compared to those of asymmetric geometries, and therefore are more promising for measuring a wider range of hydrostatic pressure, with better long-term reliability. Furthermore, a thin Parylene C layer offers improved encapsulation capability of the pressure sensor, which has stable performance for up to 72 days under large hydrostatic pressure of 10 MPa. The developed soft, flexible pressure sensor, along with other types of physical and chemical sensors[33], has the potential to be integrated with various platforms like soft robotics[53] and diver equipment for sensing under harsh ocean conditions.

4. Experimental Section

4.1 Design and fabrication of soft pressure sensors

A thin layer of poly (methyl methacrylate) (PMMA), which served as a sacrificial layer for the subsequent release of polyimide (substrate layer), was first spin coated onto a cleaned glass slide. Then, the PMMA-coated slide was spin coated (2000 rpm, 60s, 300 acceleration) with a layer of liquid polyimide, which was then pre-heated at 130 °C for 5 minutes, followed by heating of 70 minutes in a PI oven (YES-58 HMDS Oven, Yield Engineering System, Inc.) to obtain a 4 μm thick PI film. After that, magneton sputtering (AJA Orion-8 Magnetron Sputtering System, AJA International Inc.) was used to deposit a thin layer of Cr (10 nm) and Au (100 nm) on the PI, followed by photolithography and wet etching to pattern the Cr/Au layer into desired geometries of pressure sensors. Finally, another thin PI film (4 μm) on the

patterned geometries was coated as the encapsulation layer to complete the microfabrication process.

4.2 Encapsulation with Parylene C

9 g parylene C raw material was applied to coat a Parylene C film (6 μm) on the pressure sensor fabricated in section 4.1 via a Parylene C coater (Specialty Coating System, Inc.). More specifically, we first put pressure sensors in the deposition chamber of the Parylene C coater and set the chamber to vacuum conditions. Ading raw Parylene C materials to the combustion chamber and increasing temperature to 690 °C vaporized the raw Parylene C material, which was uniformly deposited onto the surface of the sensors.

4.3 Cyclic loading/unloading tests of pressure sensors

To test the performance of the pressure sensor under various pressure levels, we utilized a pressure vessel (maximum pressure: 3000 psi; Pharr Instrument Company, Moline, IL) to perform cyclic loading/unloading tests (15 cycles) in the pressure range from 0.1 to 15 MPa. A syringe pump was used to increase/decrease the amount of water in the vessel, and a pressure controller was used to control the water flow between the pump and the vessel, thereby adjusting the pressure inside the vessel. The pressure inside the vessel is monitored via a pressure gauge installed on the head of the vessel, as shown in **Figure S9**. Placing the encapsulated pressure sensor inside the vessel that was filled with deionized (DI) water started the test. To enable the recording of the testing data, two wires were soldered onto the two contact pads of the pressure sensor and then connected to data acquisition equipment through the vessel head. Epoxy (Gorilla 4200101-2 Epoxy, Gorilla USA) was used for the encapsulation

of connection wires. For each individual loading/unloading test cycle between 0.1 MPa and 15 MPa, when the inside pressure of the vessel reached the pre-set values (0.1 MPa, 3 MPa, 6 MPa, 9 MPa, 12 MPa, 15 MPa, respectively) and remained stable, a multimeter was used to record the corresponding resistance of the pressure sensor.

4.4 Bending test of pressure sensors

To perform the bending test, we first utilized a 3D printer to fabricate 6 arched molds made of digital ABS, with bending curvatures of 0, 2.50 m^{-1}, 3.43 m^{-1}, 4.24 m^{-1}, 4.91 m^{-1}, and 6.18 m^{-1}, respectively. The pressure sensor was conformally laminated onto the arched mold via a thin double-sided tape. A multimeter was used to record the resistance of the sensor under various bending curvatures. The cyclic bending test was performed by utilizing a mechanical tester (CellScale, Univert) at a loading rate of 0.5 mm/s at room temperature. In an individual test cycle (Figure 2G), the pressure sensor was held by two holders and bent into an angle of 40^{o} and then recovered its flat state. A digital multimeter was used to record the resistance change of the sensor before and after each cycle.

4.5 Test of the encapsulation capability of the Parylene C film for pressure sensors

Low-temperature solder paste (Indium Corporation) was first applied on the contact pads of the pressure sensor, and two silicone-insulated copper wires (36 AWG, 25/50 BC, Calmont Wire and Cable, INC.) were then soldered on the contact pads. The soldering areas were encapsulated by marine epoxy (Loctite marine epoxy, Henkel Corporation). Then, a parylene C film was deposited onto the sensor including the soldering area. The encapsulated sensors were then

tested inside the pressure vessel filled with DI water, under the pressure of 10 MPa, with their resistance values recorded once per day. To compare the encapsulation capability of the Parylene C film (6 μm) and pure PDMS film (100 μm), pressure sensors encapsulated with Parylene C and PDMS films were put in a plastic bellow that was filled with 35 PSU NaCl solution. The bellow was ten put in the pressure vessel filled with DI water (to minimize the contamination and potential corrosion of the pressure vessel) to test the performance of the pressure sensor under 10 MPa. A multimeter was used to record the resistance values of the sensors once per day.

4.6 Modeling

A 3D finite element model was used to compare the effects of hydrostatic pressure on a variety of sensor shapes and sizes to determine the ideal combination to maximize resistance change and underwater immersion depth without inducing plastic deformation in the gold component of the sensor. To this end, the model was used to determine the effect of pressure on the strain of the gold layer of the sensor, on which the change in resistance of the pressure sensor is dependent. The change in resistance of the pressure sensor can be determined using the maximum strain of the gold layer of the device by relating the applied strain to the gauge factor of the material as follows[54]

$$R = \rho\frac{l}{a}, \tag{1}$$

Thus

$$\frac{dR}{R} = \frac{d\rho}{\rho} + \frac{dl}{l} - \frac{da}{a}. \tag{2}$$

In (2), we have

$$\frac{d\rho}{\rho} = C\frac{dV}{V}, \tag{3}$$

where *C* is Bridgman's constant, a material property that determines the thermodynamic change in resistivity[55]. Therefore:

$$\frac{dR}{R} = \frac{dl}{l}[C(1-2v) + 1 + 2v] = G\frac{dl}{l}, \quad (4)$$

And

$$\frac{R}{R_0} = (1 + G\varepsilon), \quad (5)$$

where *G* is the gauge factor of the material, which is shown to depend on the Bridgman's constant and Poisson ratio of the material. The gauge factor of gold thin films is reported to be between 1.5 and 2.6 and depends on factors such as deposition method and grain size[56]. Thus, the change in resistance of the sensor (5) depends primarily on the gauge factor of the material and the maximum strain that is applied to it. For this analysis, the maximum principal strain on the nodes that correspond to the gold layer of the sensor and a nanocrystalline gold thin-film gauge factor of 1.5[56] were used to determine an approximate change in resistance. The results from the simulation indicate that the different sensor shapes can be exposed to hydrostatic pressures up to 15 MPa before plastic deformation occurs in the sensor, which for thin film gold is expected at around 0.53% strain[56]. The effects of loading rate could not adequately be captured within the scope of this simulation, but the behavior of the simulation and experimental results agree well overall. Experimental analysis of the gauge factor and maximum elastic strain for this particular laboratory setup could help in calculating a more accurate value to use in the conversion between applied strain and resistance change for even greater applied hydrostatic pressures.

Supporting Information

Additional experimental details, materials, and methods, including photographs of the experimental setup and results (PDF).

Acknowledgements

Y.L. S.H.L. and X.J.W. would like to acknowledge the support from the Office of Naval Research (N00014-19-1-2688 and N00014-21-1-2342). J.X. acknowledges the support from the National Science Foundation (CMMI-1762324). In addition, this work made use of the maskless aligner μMLA, which was funded by the Defense University Research Instrumentation Program from the Office of Naval Research (N00014-21-1-2223).

Competing interests

The authors declare no competing financial interests.

References

1. C. Wüthrich, G. Boschung and F. G. Toro, *Measurement: Sensors*, 2021, **18**, 100190.
2. J. Wang, Y. Zhu, Z. Wu, Y. Zhang, J. Lin, T. Chen, H. Liu, F. Wang and L. Sun, *Microsystems & Nanoengineering*, 2022, **8**, 16.
3. F. Xu, X. Li, Y. Shi, L. Li, W. Wang, L. He and R. Liu, *Micromachines*, 2018, **9**, 580.
4. R. A. S. I. Subad, L. B. Cross and K. Park, *Applied Mechanics*, 2021, **2**, 356-382.
5. Y. Cong, C. Gu, T. Zhang and Y. Gao, *Fundamental Research*, 2021, **1**, 337-345.
6. *Soft Robotics*, 2021, **8**, 625-639.
7. J. M. Nassar, S. M. Khan, S. J. Velling, A. Diaz-Gaxiola, S. F. Shaikh, N. R. Geraldi, G. A. Torres Sevilla, C. M. Duarte and M. M. Hussain, *npj Flexible Electronics*, 2018, **2**, 1-9.
8. G. Fiore, E. Anderson, C. S. Garborg, M. Murray, M. Johnson, M. J. Moore, L. Howle and K. A. Shorter, *PloS one*, 2017, **12**, e0170962.
9. A. Kaidarova, M. A. Khan, S. Amara, N. R. Geraldi, M. A. Karimi, A. Shamim, R. P. Wilson, C. M. Duarte and J. Kosel, *Advanced Engineering Materials*, 2018, **20**, 1800229.
10. J. Jijesh, M. Susmitha, M. Bhanu and P. Sindhanakeri, 2017.
11. M. Crescentini, M. Bennati and M. Tartagni, *AEU-International Journal of Electronics and Communications*, 2012, **66**, 630-635.
12. N. Brown, 1987.
13. B. Lv, H.-l. Liu, Y.-f. Hu, C.-x. Wu, J. Liu, H.-j. He, J. Chen, J. Yuan, Z.-w. Zhang and L. Cao, *Marine Georesources & Geotechnology*, 2021, **39**, 1044-1054.
14. R. Paradis and S. Wood, 2013.
15. I. Anwar, M. O. Mohsin, S. Iqbal, Z. U. Abideen, A. U. Rehman and N. Ahmed, 2016.

16. A. Bagheri, T. Karimi and N. Amanifard, *Applied Soft Computing*, 2010, **10**, 908-918.
17. J. Yuh and M. West, *Advanced Robotics*, 2001, **15**, 609-639.
18. W. Wang, J. Liu, G. Xie, L. Wen and J. Zhang, *Bioinspiration & biomimetics*, 2017, **12**, 036002.
19. D. B. Duraibabu, S. Poeggel, E. Omerdic, R. Capocci, E. Lewis, T. Newe, G. Leen, D. Toal and G. Dooly, *Sensors*, 2017, **17**, 406.
20. E. Horszczaruk and P. Brzozowski, *Construction and Building Materials*, 2014, **72**, 167-173.
21. X. Shuai, P. Zhu, W. Zeng, Y. Hu, X. Liang, Y. Zhang, R. Sun and C.-p. Wong, *ACS applied materials & interfaces*, 2017, **9**, 26314-26324.
22. Q. He, W. Zhang, T. Sheng, Z. Gong, Z. Dong, D. Zhang and Y. Jiang, *Flexible and Printed Electronics*, 2022, **7**, 045002.
23. X. Sun, S. He, Z. Qin, J. Li and F. Yao, *Composites Communications*, 2021, **26**, 100784.
24. X. Liu, Q. Zhang, F. Jia and G. Gao, *Science China Materials*, 2021, **64**, 3069-3078.
25. T. Li, G. Li, Y. Liang, T. Cheng, J. Dai, X. Yang, B. Liu, Z. Zeng, Z. Huang, Y. Luo, T. Xie and W. Yang, *Science Advances*, 2017, **3**, e1602045.
26. A. G. Kottapalli, M. Asadnia, J. Miao, G. Barbastathis and M. S. Triantafyllou, *Smart Materials and Structures*, 2012, **21**, 115030.
27. A. G. P. Kottapalli, C. W. Tan, J. Miao, G. Barbastathis and M. Triantafyllou, 2011.
28. S. C. Mannsfeld, B. C. Tee, R. M. Stoltenberg, C. V. Chen, S. Barman, B. V. Muir, A. N. Sokolov, C. Reese and Z. Bao, *Nature materials*, 2010, **9**, 859-864.
29. G.-W. Hsieh, S.-R. Ling, F.-T. Hung, P.-H. Kao and J.-B. Liu, *Nanoscale*, 2021, **13**, 6076-6086.
30. Y. S. Oh, J.-H. Kim, Z. Xie, S. Cho, H. Han, S. W. Jeon, M. Park, M. Namkoong, R. Avila and Z. Song, *Nature communications*, 2021, **12**, 1-16.
31. S. Han, J. Kim, S. M. Won, Y. Ma, D. Kang, Z. Xie, K.-T. Lee, H. U. Chung, A. Banks and S. Min, *Science translational medicine*, 2018, **10**, eaan4950.
32. E. S. Hosseini, M. Chakraborty, J. Roe, Y. Petillot and R. S. Dahiya, *IEEE Sensors Journal*, 2022, **22**, 9914-9921.
33. Y. Li, G. Wu, G. Song, S.-H. Lu, Z. Wang, H. Sun, Y. Zhang and X. Wang, *ACS sensors*, 2022, **7**, 2400-2409.
34. S.-H. Lu, Y. Li and X. S. Wang, *Journal of Materials Chemistry B*, 2023.
35. J.-M. Hsu, L. Rieth, S. Kammer, M. Orthner and F. Solzbacher, *Sensors and Materials*, 2008, **20**, 87-102.
36. S. Wu, A. Sun, Z. Lu and C. Cheng, *Materials Chemistry and Physics*, 2015, **153**, 359-364.
37. W. Chun, N. Chou, S. Cho, S. Yang and S. Kim, *Progress in Organic Coatings*, 2014, **77**, 537-547.
38. Y. Li, Y. Ma, C. Wei, H. Luan, S. Xu, M. Han, H. Zhao, C. Liang, Q. Yang and Y. Yang, *Advanced Functional Materials*, 2018, **28**, 1801380.
39. D. Zeniieh, L. Ledernez and G. Urban, *Procedia Engineering*, 2014, **87**, 1398-1401.
40. W.-C. Kuo, T.-C. Wu, C.-F. Wu and W.-C. Wang, *Materials Today Communications*, 2021, **27**, 102306.
41. M. Sasaki, W. Xu, Y. Koga, Y. Okazawa, A. Wada, I. Shimizu and T. Niidome,

Materials, 2022, **15**, 3132.
42. G. A. Bernier and D. E. Kline, *Journal of Applied Polymer Science*, 1968, **12**, 593-604.
43. S. Wang, H. Zhou, G. Dang and C. Chen, *Journal of Polymer Science Part A: Polymer Chemistry*, 2009, **47**, 2024-2031.
44. S. Numata and T. Miwa, *Polymer*, 1989, **30**, 1170-1174.
45. A. Al-Halhouli, I. Kampen, T. Krah and S. Büttgenbach, *Microelectronic engineering*, 2008, **85**, 942-944.
46. M. Hopcroft, T. Kramer, G. Kim, K. Takashima, Y. Higo, D. Moore and J. Brugger, *Fatigue & Fracture of Engineering Materials & Structures*, 2005, **28**, 735-742.
47. J. Gao, L. Guan and J. Chu, 2010.
48. M. Shaat and A. Abdelkefi, *Journal of Applied Physics*, 2016, **120**, 235104.
49. L. Wang and B. Prorok, *Journal of Materials Research*, 2008, **23**, 55-65.
50. I. Miranda, A. Souza, P. Sousa, J. Ribeiro, E. M. Castanheira, R. Lima and G. Minas, *Journal of Functional Biomaterials*, 2021, **13**, 2.
51. J. Oh, J.-H. Kim, S. Y. Lee, M. S. Kim, J. M. Kim, K. Park and Y.-S. Kim, *IEEE Transactions on Device and Materials Reliability*, 2017, **18**, 1-4.
52. Y. Zhang, D. Wen, M. Liu, Y. Li, Y. Lin, K. Cao, F. Yang and R. Chen, *Advanced Materials Interfaces*, 2022, **9**, 2101857.
53. G. Li, X. Chen, F. Zhou, Y. Liang, Y. Xiao, X. Cao, Z. Zhang, M. Zhang, B. Wu, S. Yin, Y. Xu, H. Fan, Z. Chen, W. Song, W. Yang, B. Pan, J. Hou, W. Zou, S. He, X. Yang, G. Mao, Z. Jia, H. Zhou, T. Li, S. Qu, Z. Xu, Z. Huang, Y. Luo, T. Xie, J. Gu, S. Zhu and W. Yang, *Nature*, 2021, **591**, 66-71.
54. S. Zike and L. P. Mikkelsen, *Experimental Mechanics*, 2014, **54**, 393-403.
55. P. W. Bridgman, *Physical Review*, 1914, **3**, 273.
56. C. Li, P. Hesketh and G. Maclay, *Journal of Vacuum Science & Technology A: Vacuum, Surfaces, and Films*, 1994, **12**, 813-819.

Figures

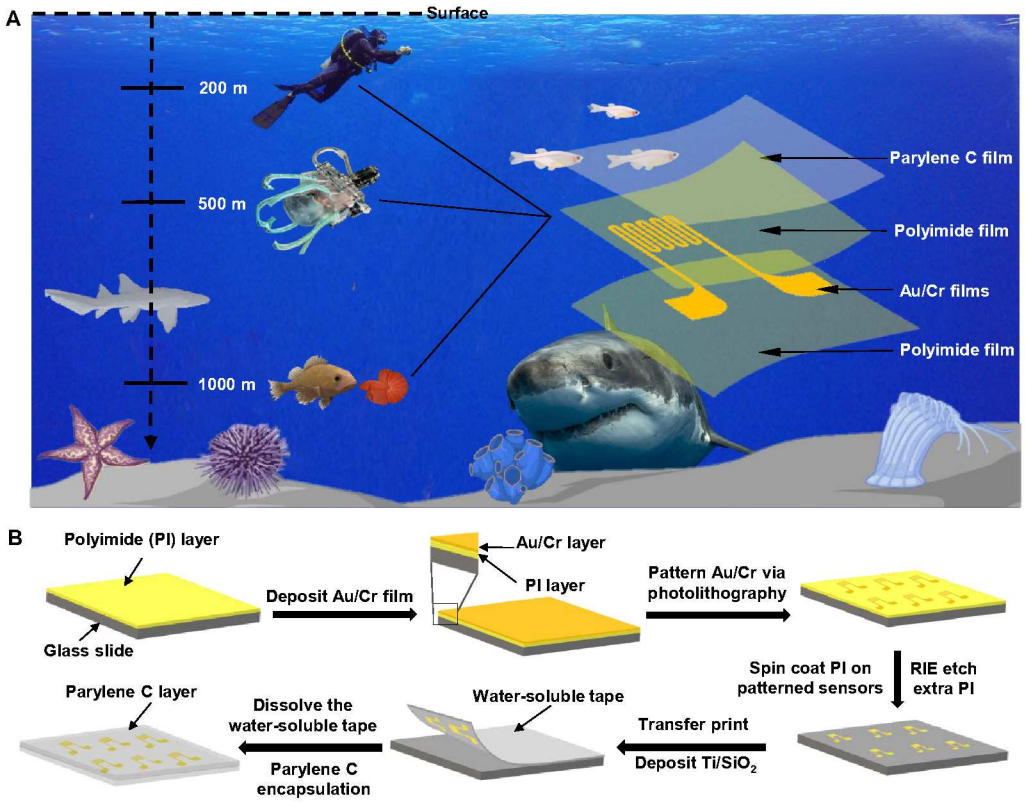

Figure 1. Schematic illustration of (A) soft pressure sensors for integration with diverse platforms for applications in the ocean environment, and (B) fabrication schemes of soft pressure sensors.

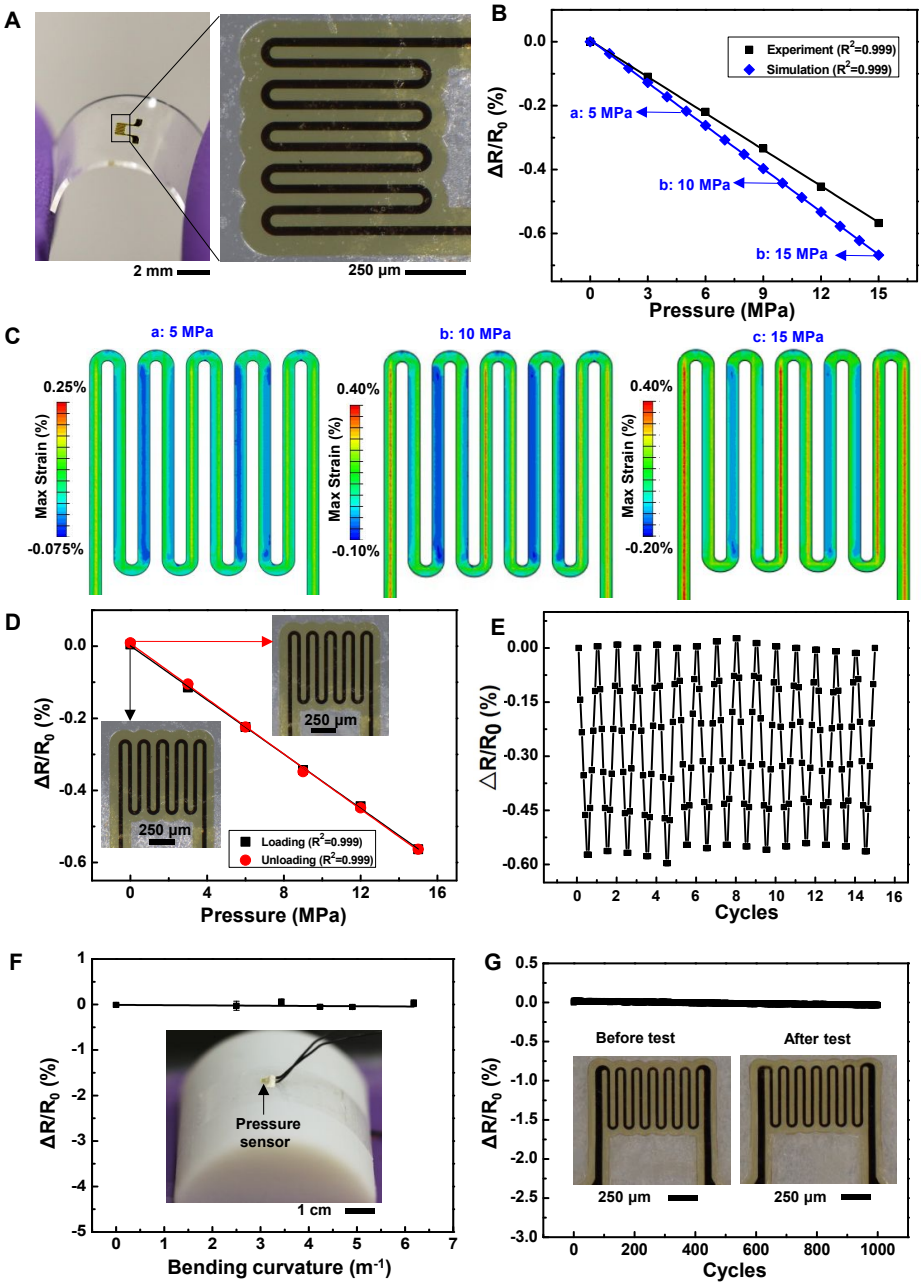

Figure 2. Characterizations of soft rectangular pressure sensors. (A) Optical images of the soft pressure sensor held by two hands. (B) Experimental and simulation results of fractional resistance change of the rectangular pressure sensor as the hydrostatic pressure increases from 0.1 MPa to 15 MPa. (C) Finite element analysis of strain distributions in the pressure sensor under 5 MPa, 10 MPa, and 15 MPa, respectively. (D) Fractional resistance change of the pressure sensor under one cycle of loading/unloading between hydrostatic pressure of 0.1 MPa and 15 MPa, with optical microscope images of the sensor before and after testing. (E) Cyclic loading test of the rectangular sensor. (F) Fractional resistance change of the pressure sensor as a function of bending curvatures (n=3). (G) Fractional resistance change of the pressure sensor over 1000 cycles of a mechanical bending test.

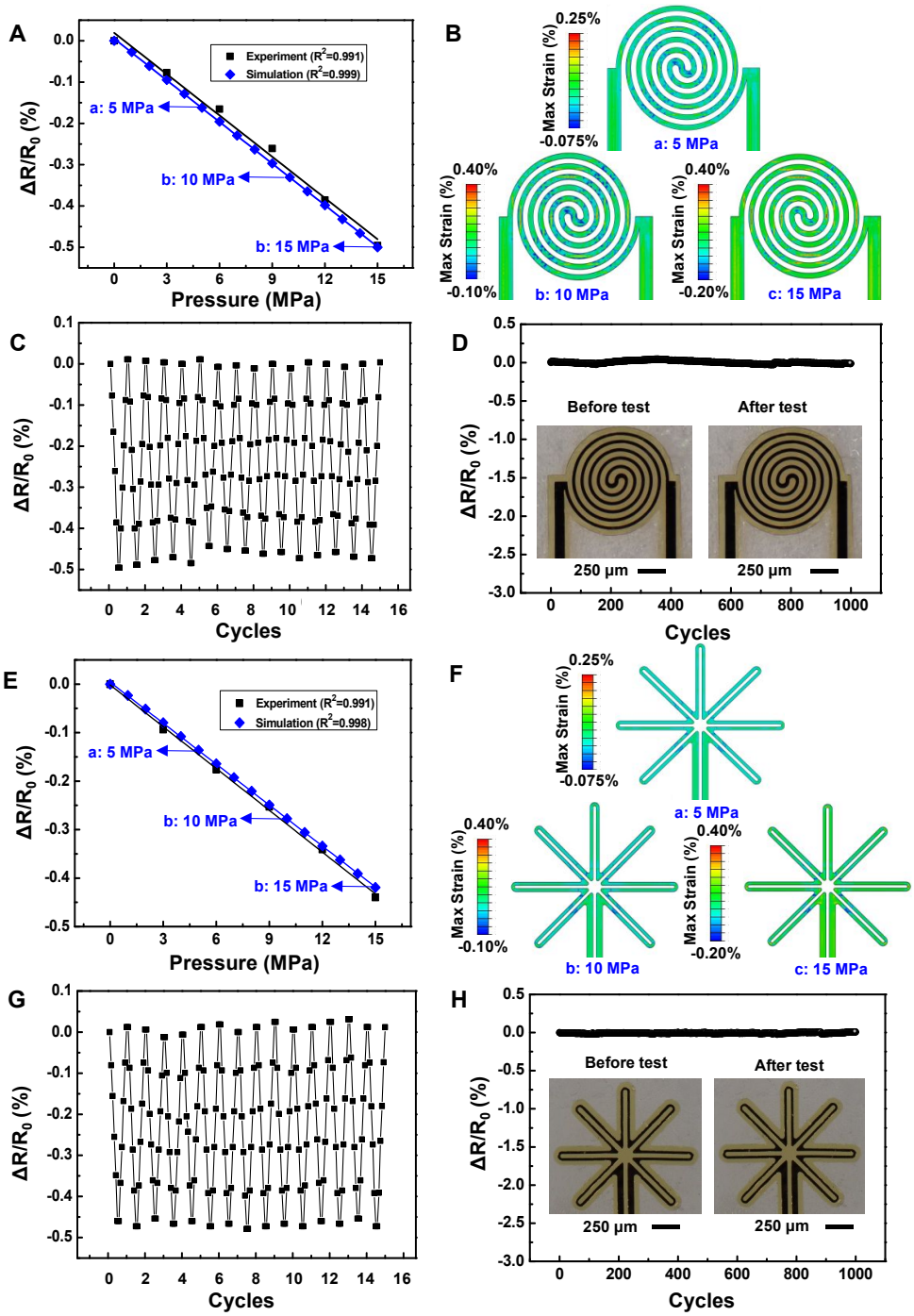

Figure 3. Effect of sensor geometry on the performance of the pressure sensor. (A, E) Experimental and simulation results of the fractional resistance change of a circular (A) and spike-shaped (E) sensor under hydrostatic pressures of 0.1-15 MPa. (B, F) FEA prediction of strain distributions within the circular (B) and spike-shaped (F) pressure sensor under 5 MPa, 10 MPa and 15 MPa, respectively. (C, G) Cyclic loading/unloading test of the circular (C) and spike-shaped (G) pressure sensor with circular shape. (D, F) Cyclic bending behaviors of the circular (D) and spike-shaped (F) pressure sensor over 1000 cycles, with corresponding optical

microscope images of the sensor before and after test.

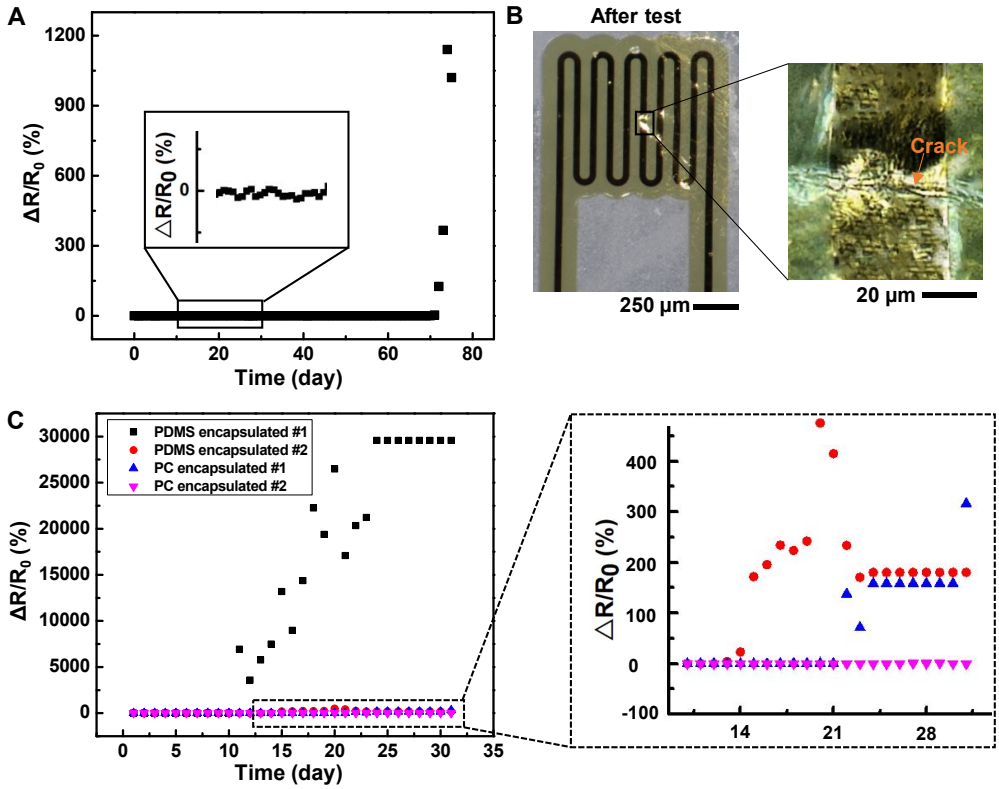

Figure 4. Encapsulation capability of the soft pressure sensor. (A) Fractional resistance change of a rectangular pressure sensor tested under a hydrostatic pressure of 10 MPa in the pressure vessel filled with DI water. (B) Optical microscope images of the rectangular sensor after test. (C) Comparison between the encapsulation capabilities of PDMS film and Parylene C film for pressure sensors in 35 PSU and 10 MPa conditions in the pressure vessel.